ADVANCED FUNCTIONAL MATERIALS
www.afm-journal.de

Structurally Colored Physically Unclonable Functions with Ultra-Rich and Stable Encoding Capacity

Abidin Esidir, Miaoning Ren, Sami Pekdemir, Mustafa Kalay, Nilgun Kayaci, Nail Gunaltay, Hakan Usta, Xian Huang, and Mustafa Serdar Onses**

Identity security and counterfeiting assume a critical importance in the digitized world. An effective approach to addressing these issues is the use of physically unclonable functions (PUFs). The overarching challenge is a simultaneous combination of extremely high encoding capacity, stable operation, practical fabrication, and a widely available readout mechanism. Herein this challenge is addressed by designing an optical PUF via exploiting the thickness-dependent structural color formation in nanoscopic films of ZnO. The structural coloration ensures authentication using widely available bright-field-based optical readout, whereas the metal oxide provides a high degree of structural stability. True physical randomness in spatial position is achieved by physical vapor deposition of ZnO through stencil masks that are fabricated by pore formation in polycarbonate membranes via photothermal processing of stochastically positioned plasmonic nanoparticles. Structural coloration emerges from thin film interference as confirmed via simulation studies. The rich color variation and stochastic definition of domain size and geometry result in chaotic features with an encoding capacity that approaches $(6.4 \times 10^5)^{(2752\times2208)}$. Deep learning-based authentication is further demonstrated by transforming these chaotic features into unbreakable codes without field limitations. This ultra-rich encoding capacity, coupled with outstanding thermal and chemical stability, forms a new cutting edge for state-of-the-art PUF-based encoding systems.

1. Introduction

Despite the presence of deterrent legislation worldwide, counterfeiting and copyright infringement remain major global issues, posing economic and health threats in a wide range of industries, including pharmaceuticals, footwear, food, and electronics.[1] In addition, ensuring data security and safeguarding digital communication require the use of advanced cryptographic key generation methods. Conventional anti-counterfeiting methods (e.g., watermarks, holograms, graphic barcodes, and security inks) and digital security technologies have become inadequate due to their deterministic nature, which makes them vulnerable to undesired replication and attacks.[1] In today's highly digitalized world, an unconventional and promising encoding solution has recently emerged based on using physical systems, which indeed have been in use since ancient times.[2] These systems are known as physically unclonable functions (PUFs), and they rely on physical processes that

A. Esidir, S. Pekdemir, M. Kalay, N. Gunaltay, M. S. Onses
ERNAM – Nanotechnology Research and Application Center
Erciyes University
Kayseri 38039, Turkey
E-mail: onses@erciyes.edu.tr

A. Esidir, M. S. Onses
Department of Materials Science and Engineering
Erciyes University
Kayseri 38039, Turkey

A. Esidir
The Scientific and Technological Research Council of Turkey
Ankara 06680, Turkey

A. Esidir
Erciyes University
Graduate School of Natural and Applied Science
Materials Science and Engineering Program
Kayseri 38039, Turkey

M. Ren, X. Huang
School of Precision Instrument and Optoelectronics Engineering
Tianjin University
Tianjin 300072, China
E-mail: huangxian@tju.edu.cn

M. Ren, X. Huang
State Key Laboratory of Precision Measuring Technology and Instruments
Tianjin University
Tianjin 300072, China

The ORCID identification number(s) for the author(s) of this article can be found under https://doi.org/10.1002/adfm.202417673

DOI: 10.1002/adfm.202417673

generate random and unique responses to applied challenges.[3,4] The rapid development of PUFs over the past years has been made possible by the advent of new, suitable materials and fabrication methods. In this context, we have recently seen a significant expansion in the types of materials explored for use in PUFs. Notable examples include quantum dots,[5,6] perovskite nanocrystals,[7] plasmonic nanoparticles,[8,9] nanowires,[10] organic semiconductors,[11] graphene,[12] embedded nanostructures,[13] food-grade starch,[14] polymeric particles,[15] self-assembled polymers,[16] and synthetic materials based on self-wrinkling.[17] Therefore, continuous efforts with new materials and fabrication methods are essential to further explore and advance PUF-based encoding systems.

High encoding capacity, practical read-out, and stable operation are essential for the practical implementation of PUFs in real-world applications. Additionally, high-throughput production and the capability to generate a large number of keys are critical for realizing a strong PUF. This capability not only enables the assignment of unique keys to a large body of entities, including physical objects and digital systems, but also makes the encoding system highly resistant to undesired attacks. Encoding capacity refers to the maximum number of keys that can be generated, defined by R^n, where R is the number of possible responses and n represents the number of independent variables for a given key length. The most effective strategy to increase the encoding capacity of a PUF is to maximize R, rather than relying on binary encoding (i.e., where R would be 2).[18] A commonly adopted and effective approach to this end is to employ various forms of optical phenomena, which results in multiple independent responses on the same PUF. In a typical example, multiple photoluminescent materials are randomly positioned on a substrate to generate multicolor fluorescence images.[18] In other examples, Raman scattering from molecules[19] and dark-field scattering from plasmonic nanoparticles with anisotropic geometries enable the generation of multiple responses within a single image.[20] However, it is important to note that the implementation of these optical techniques is contingent upon access to specialized, advanced infrastructure, which is not widely available, particularly for individual customer applications of PUFs on physical objects. Furthermore, the associated materials and responses are not stable under harsh temperatures and chemical conditions. Therefore, while these approaches are effective in achieving high-encoding capacity, they fall short in addressing practical read-out and stability aspects. In terms of practical and highly accessible read-out methods, bright-field optical imaging is clearly the most prominent method. The accelerated advancement of high-precision smartphone cameras over the past decade serves as a promising indicator of the extensive accessibility of this technology.[21] However, the majority of the optical PUFs that are resolvable under a bright-field optical microscope have relatively low encoding capacity, as they typically rely on a binary response with an R value of 2.[22,23] Therefore, it is crucial to enhance the variety of optical challenge-response pairs (i.e., increase the R value) by using new materials and positioning them effectively at the optimal length scales on a substrate to achieve a large n value.

Structural color formation is an effective way to substantially enhance the encoding capacity of features in bright-field resolvable optical systems. Inspired by natural organisms, structural coloration emerges from the light-matter interactions at small length scales. This structure-dependent color formation has been exploited for the fabrication of deterministic security labels in anti-counterfeiting applications.[24] Adapting structural coloration through stochastic physical processes could be a very effective approach to fabricate bright-field resolvable PUFs with high encoding capacity. Structural color-based PUFs have recently garnered significant interest owing to their unpredictable chaotic nature and potential for multi-color coding. An earlier report exploited pH-driven transformation in a homogeneous polymer thin film, leading to the formation of a network of folded domains that exhibit structural colors. These networks were further decorated with metallic nanoparticles to impart surface-enhanced Raman scattering activity.[25] With their intriguing optical properties, liquid crystal domains positioned at random spatial positions have recently been explored for constructing PUFs.[26,27] In these studies, liquid crystals were confined and stabilized within polymeric droplets, and the reported range of achievable colors was not substantially high. On the other hand, the need for polarized optical microscopes and the liquid nature of the materials challenge practical applications that require high-temperature stability. Han et al.[28] exploited thickness-dependent color formation in thin films of a coordination polymer, in which the random formation of microscale crystals with varying thicknesses resulted in bright-field readable multi-color images to construct PUF-based security labels. In another example, structural color-based multi-level encoded surfaces were prepared by amorphous photonic structures composed of nanoparticles coupled with an intermediate layer that undergoes wetting-induced transitions. To construct a PUF with these photonic structures, the local variations in the structural color were decoded using an artificial intelligence-based recognition algorithm. In a recent relevant work, ink-jet printing of polymeric nanospheres[30] on a substrate composed of black paper yielded structural color formation due to scattering of light. Despite the uniform colors at the macroscopic scale, randomly positioned microscale domains within the printed regions displayed variations in hue. The formation of randomly positioned and oriented cracks in films of colloidal crystals is another approach to constructing PUFs with structural

S. Pekdemir
Department of Aeronautical Engineering
Faculty of Aeronautics and Astronautics
Erciyes University
Kayseri 38039, Turkey
M. Kalay
Department of Electricity and Energy
Kayseri University
Kayseri 38039, Turkey
N. Kayaci, H. Usta
Department of Materials Science and Nanotechnology Engineering
Abdullah Gül University
Kayseri 38080, Turkey
M. S. Onses
UNAM-National Nanotechnology Research Center
Institute of Materials Science and Nanotechnology
Bilkent University
Ankara 06800, Turkey

color.[31] Although more advanced instrumentation is required, it is possible to create photonic crystals with bright-field resolvable structural color responses by subjecting graphene/gold nanostructures to femtosecond laser treatment.[32] Femtosecond-laser treatment of metallic thin films can also generate multi-color responses that can be read out in dark-field imaging.[33] Photonic crystals based on ordered assemblies of colloidal particles are an established route to generate structural colors. Randomized flow,[34] electrostatic fields,[35] and combination with fluorescence[36] have recently been demonstrated on photonic crystals to generate high encoding capacity multi-color PUFs. Cellulose nanocrystals from natural sources offer structural coloring based PUFs with biocompatibility and biodegradability.[37] The responsive nature[38] of such photonic crystals further enables multi-layered encoding.[39] Overall, these studies have demonstrated the effective generation of structural color-based PUFs using a diverse range of materials and fabrication methods. Given the current state of the art in this field, fabricating structural color-based PUFs with extremely high encoding capacity using robust materials with stable responses remains a formidable challenge.

In this study, we report a unique design strategy to generate structurally colored chaotic inorganic features with extremely rich and stable responses that can be read out via bright-field optical imaging. Central to this strategy is the thickness-dependent color generation in metal oxide thin films. Structural color formation in thin films provides access to a broad range of colors with extremely high levels of stability. Metal oxides particularly stand out with their stability and well-studied thin film behaviors. We choose ZnO because it effectively forms structural colors across the entire visible spectrum,[40,41] Furthermore, thin films of ZnO can be easily and cost-effectively fabricated via conventional physical vapor deposition (PVD) methods. To generate multi-color response ZnO features with random positions and colors, we used stencil masks fabricated through a physical and stochastic process. Randomly positioned microscale holes with diverse sizes and geometries were opened in a free-standing film of a polycarbonate (PC) membrane by using a photothermal process facilitated via intense pulsed light (IPL).[42] Randomly positioned nanoparticles mediate localized heating and melting of the membrane, leading to the chaotic formation of physical holes. Using this modified PC membrane on a silicon substrate as a stencil mask, PVD of ZnO leads to the formation of random metal oxide features on the substrate. The color of these features is determined by the thickness of the ZnO layer, as confirmed by experimental and simulation studies. Unclonable ZnO features with extremely rich colorful responses are obtained by repeating the PVD process using two different membranes. To fully benefit from the chaotic surface features with diverse colors, an artificial intelligence-based authentication algorithm was employed. In comparison to the most widely utilized binary keys with an R-value of 2, our approach achieves an R value of 6.4×10^5. The response of the fabricated PUFs remains unaltered even after exposure to elevated temperatures of 500 °C and harsh organic solvents. The generation of bright-field resolvable optical responses at such an enormous richness, combined with high-temperature stability, represents a significant advancement in the field.

2. Result and Discussion

2.1. Fabrication and Characterization of Structurally Colored PUFs

Figure 1 illustrates our approach in the design and fabrication of structurally colored, unclonable ZnO features with ultra-rich and stable encoding capacity. Our approach is based on the repetitive use of PC membranes possessing randomized holes as stencil masks and the RF magnetron sputtering of ZnO through the stencil masks. The randomized hole formation in the stencil mask was accomplished through plasmonic heating of silver nanoparticles (AgNPs) dispersed randomly on a PC membrane, resulting in localized thermal effects and induced perforation using the AgNPs as templates (Figure 1a). The fabrication of holes in the PC membrane is a purely physical and stochastic process that can be conducted in a regular lab environment. This free-standing membrane is then transferred (Figure 1b) onto the target Si substrate by using a supportive copper foil (see Figure S1, Supporting Information for details). Direct PVD of ZnO (Figure 1c) leads to the formation of structurally colored random features (Figure 1d). The structural coloration depends on the thickness of ZnO as confirmed by optical measurements performed on unpatterned films with a thickness ranging from 160 to 290 nm (Figure 1e). To enhance the achievable range of colors and the lateral distribution of metal oxide features, we repeated the ZnO deposition on the same substrate by using two different stencil masks, each produced through a separate stochastics process. This process not only generated multiple colors with extremely high encoding capacity but also further enhanced the randomness of the surface, which makes the duplication practically impossible. Here, we note that the PC stencil masks used in our study have randomly formed non-uniform openings, which is crucial for the formation of ZnO features with varied thicknesses. In a typical process, we performed consecutive depositions of 160 and 150 nm-thick ZnO layers through two different PC stencil masks. At this point, we noticed that even the bare eye can identify the significant enhancement in the range of colors following the second deposition process (Figure 1d). Owing to the openings of the membranes at random positions and with varied geometries, the surface of the silicon substrate exhibited a highly heterogeneous thickness distribution after the two-layer deposition. The excellent variation in thickness is also the result of ZnO domain formation at nano-scales and geometric factors (e.g., the shadowing effect of the opening in the stencil mask) that interfere with the sputtering process. Although 150–160 nm thickness was employed in our study, we note that the thickness values can be varied by the manufacturer, without making any major change in the deposited ZnO properties (vide supra), to fabricate different PUF labels.

The resulting chaotic features are digitized using a neural network-based algorithm. To fully utilize the chaotic and highly detailed color information in the images, special consideration is needed for the authentication process. To this end, a bag of features (BoF) approach was employed to encode each image in the training set (Figure 1f). In this approach, the function detects, and extracts features in the image, and then utilizes the approximate nearest neighbor algorithm to create a feature histogram. The function subsequently increments the histogram bins based

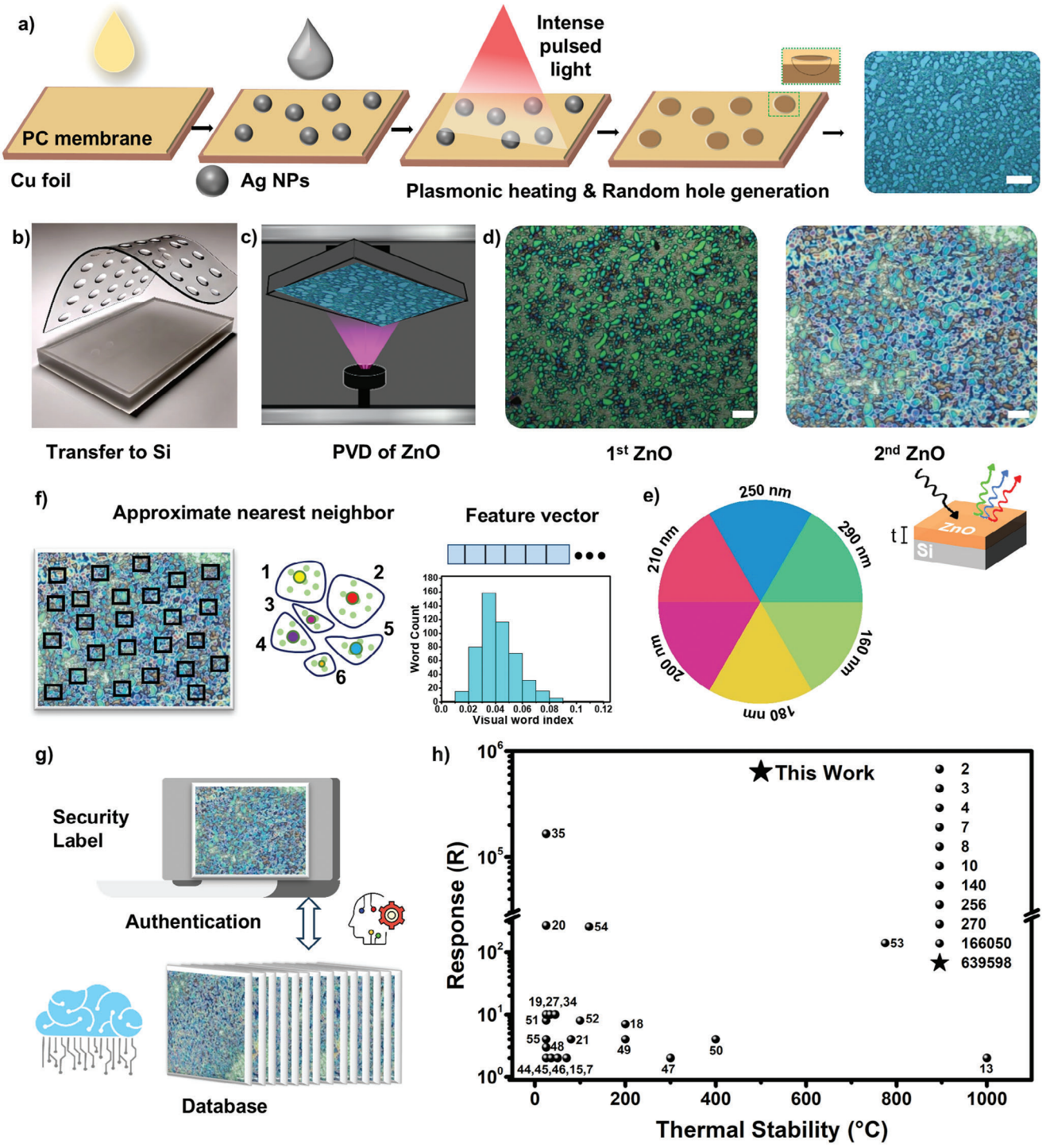

Figure 1. Structurally colored PUFs. a) Schematic fabrication of a PC stencil mask with randomly positioned holes and an optical microscope image. Scale bar is 100 µm. b) Transfer of the free-standing mask onto a silicon substrate. c) Deposition of ZnO, d) Optical microscopy images a silicon substrate following deposition of 160 nm thick ZnO through the first membrane, and the same substrate after the additional deposition of 150 nm ZnO through a different membrane. Scale bars are 100 µm. e) Thickness dependent structural coloration. Presented are optical microscopy images of ZnO films with different thicknesses. f) Artificial intelligence mediated digitization of the images. g) Schematic for the authentication process. h) Comparison of the number of responses and highest temperature that PUF can withstand with the literature.[7,13,15,18–21,27,34,35,44–55]

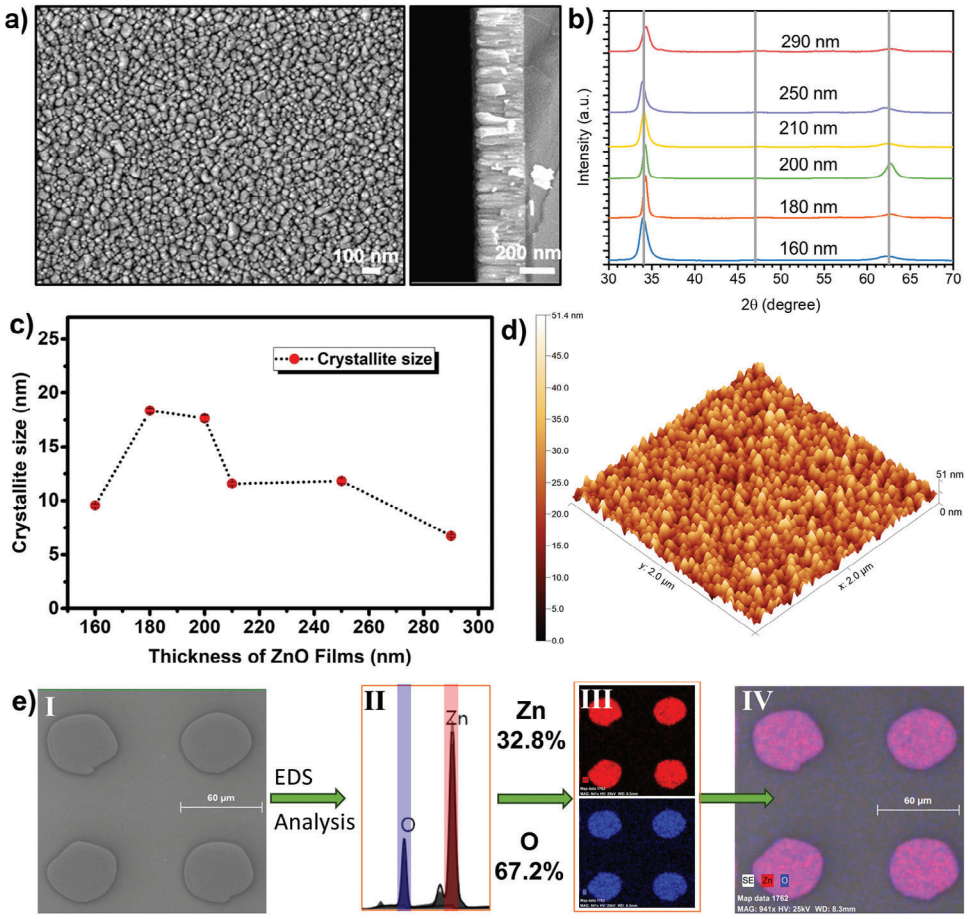

Figure 2. Microstructural and morphological characterizations of deposited ZnO films and features. a) Top-view and cross-sectional SEM images of a 200 nm ZnO thin film. b) XRD analysis of ZnO thin films of various thicknesses. c) Graphical representation of the variation of the crystallite size with the thickness of the film. d) AFM image of a 200 nm thick ZnO thin film. e) EDX analysis and mapping of patterned ZnO film structures: I) SEM image of the EDX mapping area, II) EDX spectrum labeled with Zn and O, III) ED mapping image based on Zn (top) and O (bottom). IV) Composite image obtained by merging EDX mapping and SEM images.

on the proximity of the descriptor to a specific cluster center. The length of the histogram corresponds to the number of visual words generated by the BoF object. The histogram transforms into a feature vector for the image. This step is repeated for each image to generate the training data. The classifier is then tested against the validation image set.[43] The authenticity of a label is facilitated by matching of features in the images captured by the user and those stored in the database (Figure 1g).

Collectively, the presented design strategy enables a unique combination of extremely rich encoding capacity and robustness (Figure 1h). The encoding capacity of the surface stems from three distinct phenomena: i) variation in ZnO film thickness can generate various structural colors through the thin-film interference effect, ii) crystalline, nano-sized ZnO grains grown at random locations on the substrate through a stencil mask can enhance lateral resolution and structural color variation, and iii) multiple uses of stencil masks, each generated through a stochastic process, can further enhance the randomness in the domain thickness and locations on the surface. The employment of a robust inorganic material with a very high bulk melting point (1975 °C) is key in constructing a robust PUF system.

Figure 2 presents the structural characterization of the ZnO films deposited at varied thicknesses (160, 180, 200, 210, 250, and 290 nm). All ZnO thin-films were found to be crystalline, consisting of homogeneous and highly interconnected nano-sized (≈20–100 nm) granular domains (additional images are provided in Figures S2, Supporting Information). Based on the cross-sectional scanning electron microscope (SEM) images, the ZnO structures are shown to grow in columnar islands perpendicular to the substrate plane (i.e., Volmer–Weber-type growth).[56] The granular domain size observed with top-view SEM images corresponds to the lateral size of these columnar structures, which changes with the film thickness. As the film thickness increases from 160 to 290 nm, the granular domain size increases from ≈20 to ≈100 nm. Atomic force micrsocope (AFM) imaging (Figure 2d; Figure S3, Supporting Information) further confirms the morphology of these columnar features, showing cone-like structures on the top surface with dimensions similar to those observed in the SEM images. The root-mean-square roughness becomes higher as the film thickness increased (Figure S4, Supporting Information), a well-known outcome for films deposited by PVD processes.[57] The roughness values for the films

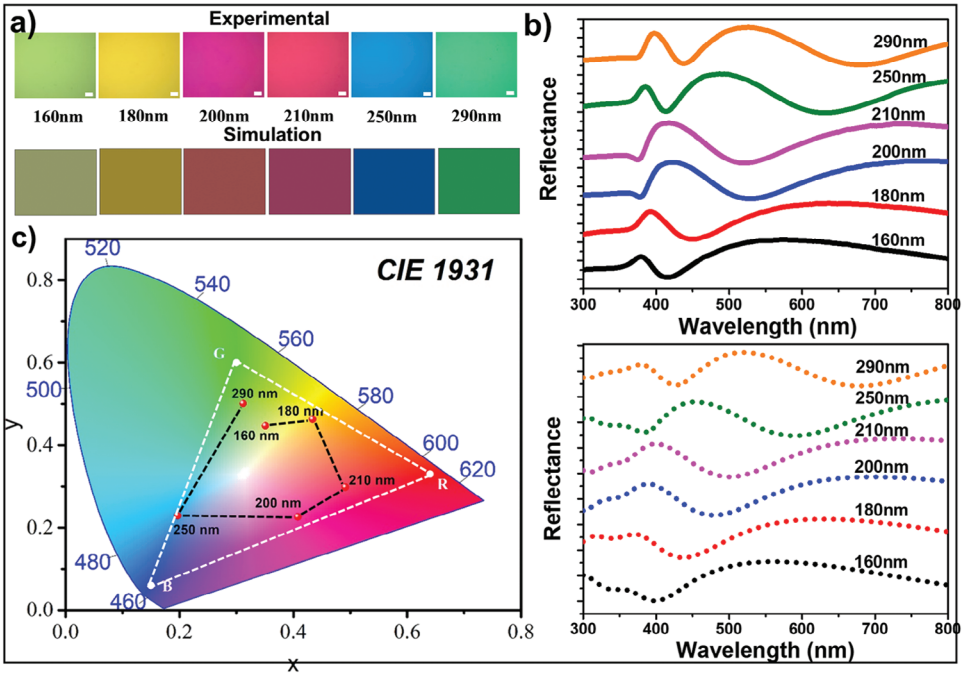

Figure 3. Generated structural colors and reflection spectra. Shown are the a) structural colors in the experiment (top row) and the simulation (bottom row) as a function of deposited ZnO film thickness (Scale bars 100 µm). b) The measured (top panel) and simulated (bottom panel) reflectance spectra of the thin films as a function of deposited ZnO film thickness. c) The chromaticity diagram on the CIE 1931 scale. The standard sRGB color triangle is also shown. The obtained structural color coordinates (red spots) are connected for easy visualization of the trend as a function of deposited ZnO thickness.

are measured to be less than 10 nm, which is orders of magnitude smaller than the wavelength of visible light. Therefore, the effect of roughness on the structural color formation is insignificant. The X-ray diffraction (XRD) peaks observed at 34.2° and 62.6° (Figure 2b) indicate that the crystallographic planes of (002) and (130) are assigned to be oriented on the substrate surface. These findings not only substantiate the existence of the wurtzite hexagonal crystal structure.[58] but also suggest the preferential out-of-plane growth of ZnO grains mainly along the [002] crystallographic direction. This crystal alignment preference observed during the sputtering process may be attributed to the (002) plane's lower surface energy as compared to other crystalline planes. The coherence lengths (i.e., extent of ordering) in the out-of-plane direction, also referred to as crystallite size in general, were calculated from the (002) XRD peak using the Debye–Scherrer equation (Equation S1, Supporting Information).[59] The calculated crystallite sizes, ranging from 6 to 19 nm (Figure 2c), indicate that the granular features observed in the SEM images correspond to multiple crystallites. The small variation in the crystallite size can be attributed to the growth over different crystallographic planes with the increasing thickness of the film and has negligible effect on the structural color formation. SEM and energy dispersive X-ray spectroscopy (EDX) mapping images of ZnO patterns prepared by lithography for the stability experiments are given in Figures 2e and S5 (Supporting Information). EDX analysis shows a stoichiometric composition of 32.8% zinc and 67.2% oxygen. All these morphological and microstructural analyses prior to the PUF fabrication clearly show that the RF magnetron sputtering of ZnO films at varied thicknesses (160–290 nm) can potentially yield crystalline, nanostructured films with a high lateral resolution, which could potentially contribute to rich structural color formation for realizing a high encoding capacity.

Vibrant structural colors can be generated employing either random[60] or periodic arrays of dielectric and plasmonic nanostructures called metamaterials or photonic crystals,[28,41,61] and multilayer thin films.[40,62,63] A simple process to generate structural color is depositing a thin dielectric film on a medium with a high reflective index, such as silicon.[62,64] In such cases, the optical path difference (OPD) between the light beam directly reflected from the air-thin film interface and the thin film-Si interface modulates the intensity of the reflected light being observed. When the OPD is integer multiples of the incident wavelength (1λ, 2λ, 3λ, etc.), constructive interference occurs, resulting in maximum reflectance; when the OPD is half-odd-integer multiples of the incident wavelength ($1/2\lambda$, $3/2\ \lambda$, $5/2\ \lambda$, etc.), a destructive interference results, leading to minimum reflectance. For a broadband incident light source, as used in this study, the interference patterns result in multiple peaks and troughs in the reflectance spectrum of the thin film, displaying various colors depending on thickness.[62]

The reflectance spectra of the deposited ZnO thin films were simulated using the generalized transfer matrix method for thicknesses ranging from 160 to 290 nm to obtain various colors (**Figure 3**). As thickness increases, the color changes in the order of yellow green, gold, magenta, deep pink, deep blue, and turquoise (Figure 3a). Similarly, the simulated reflectance and absorbance spectra exhibits multiple maximums and minimums,

the number of which increases from 160 nm-thick ZnO film to 290 nm-thick film (Figure 3b; Figure S6, Supporting Information). For example, there are two peaks at 550 nm/390 nm and a trough at 420 nm in the reflectance spectrum of 160 nm-thick ZnO film. As the film thickness increases, both the maximum and minimum peak positions shift to longer wavelengths while the higher-order peaks and troughs disappear. For instance, in the reflectance spectrum of the thickest (290 nm) ZnO film, the primary peak is outside the measurement range (up to 800 nm), and the high-order peaks appear at 520 nm/400 nm while the troughs appear at 680 nm/420 nm. The simulated spectrum and color of the thin films as a function of thickness confirm that the displayed colors are due to thin film interference as mentioned earlier. The slight mismatch between the simulated and the experimental results is due to the use of wavelength-dependent refractive indices for simulation, which are derived from ZnO thin films deposited by a spray pyrolysis method.[65] Our experimental and simulation results suggest that film thickness is the key parameter determining the structural color. A color chromaticity diagram can be used to evaluate the range of colors that can be generated using the fabricated ZnO thin films. Figure 3c shows the color chromaticity diagram on the CIE 1931 scale of the obtained colors (red spots) and the standard sRGB color range (dashed triangle). The color coordinates of the films form a clockwise spiral as the film thickness increases from 160 to 290 nm, similar to earlier observations.[40,64] The resulting color gamut is relatively broad (50%) and it compares well to previous studies.[32,41,64] It should be noted that structural colors with a broader gamut than the sRGB have been generated in many previous researches,[61,66–68] albeit the complex processes, including the deposition of multilayers and the fabrication of photonic crystals, limit their practical application as convenient PUF tags.

2.2. Randomness Analysis and Authentication of Structurally Colored PUFs

To substantiate the chaotic formation of features, a randomness analysis was conducted using the tests delineated by the National Institute of Standards and Technology (NIST). These tests operate on binary bits, which are composed of 0-bits and 1-bits. Therefore, optical images of structurally colored PUFs were binarized for the randomness analysis. The NIST tests were applied to 7680 bits of digitized keys derived from 30 different images. A total of 60 sequences, each consisting of 128 bits, were analyzed using the frequency, frequency within a block, runs, longest run of ones, serial, approximate entropy, and cumulative sums tests (see upporting information for additional details). A p-value threshold of ≥ 0.01 was employed to ascertain the randomness of the binary keys, and a pass rate of at least 56 out of 60 sequences was required for each test to be deemed successful. The results of all seven tests (Table S1, Supporting Information) demonstrated that the binary keys derived from fabricated PUFs exhibited randomness.

A deep learning-based authentication algorithm effectively and rapidly recognizes genuine and fake labels. Conventional authentication protocols typically rely on the comparison of digitized binary keys. Applying this approach to multi-color PUFs would result in an excessive loss of useful information for colorful PUFs with extremely rich responses. ZnO PUFs possess color and textural features that are not easily distinguishable through visual inspection. Therefore, a solution independent of color, shape, and texture features is needed for classification. In this study, a deep convolutional network was employed to reveal and classify random patterns in these images (**Figure 4**). A series of processes have been undertaken to recognize and decode ZnO PUFs using convolutional neural networks (CNNs), which are particularly powerful for the robust extraction of image features.[69,70] The accurate and rapid recognition of genuine and fake labels is critical for a successful authentication process. A database is first constructed by using images of genuine samples (Figure 4a). In practical settings, images can be taken under nonideal conditions with distortions in characteristics such as size, brightness, and rotation (Figure 4b). Images of other samples that are labeled as fakes are also captured (Figure 4c). To study authentication via the deep-learning algorithm, we used a dataset consisting of 1000 images of structurally colored PUFs, which were taken from genuine samples under diverse conditions with varied brightness, rotation, and sizing (Figure S7, Supporting Information). Of these images, 80% were used for training and 20% were used for validation. The training set was used to feed the algorithm to build a generalized model, while the test set evaluated the performance of the model against unknown data. A BoF technique was used to extract features from the training images. The images of ZnO PUFs fed the ResNet-50 architecture as an image data repository. Learning was expedited by incorporating limitations into the dataset to understand the features of images taken under different conditions. The program matrix requires an image data size of $224 \times 224 \times 3$, in which the dimension parameters represent the width, height, and color channel of the input RGB images, respectively. During training, the images were classified by ResNet-50 using a network, and the classification accuracy rate was calculated. Test images were continuously looped through the system, and the loop was organized to make the most accurate predictions. After the training phase, the test image set was evaluated to assess the accuracy of the machine learning model. In this study, an average accuracy rate of ≈91% was achieved in distinguishing genuine labels from fake labels (Figure 4d). The artificial intelligence-based deep learning algorithm was successful in recognizing genuine samples in descending order from images with brightness, rotation, and size (Figure 4e; Figure S8, Supporting Information). The recognition of a single image from a database comprising 1000 images was completed in less than 300 ms using a standard laptop computer. The authentication time is contingent upon the size of the database, the processing power of the computer, the number of security layers, and the duration of image capture. Benefiting from the high encoding capacity will require the generation of a larger database, which will consequently lead to longer recognition times. The similarity rates (see supporting information for details) for the genuine samples imaged under different conditions were close to 1.0, whereas this value was below 0.2 for the fake samples (Figure S9, Supporting Information).

To fully benefit from the rich structural color-based encoding, we propose quantitative color matching as a second layer of authentication. This security layer directly and solely probes the color differences in selected pixels. For this purpose, regions

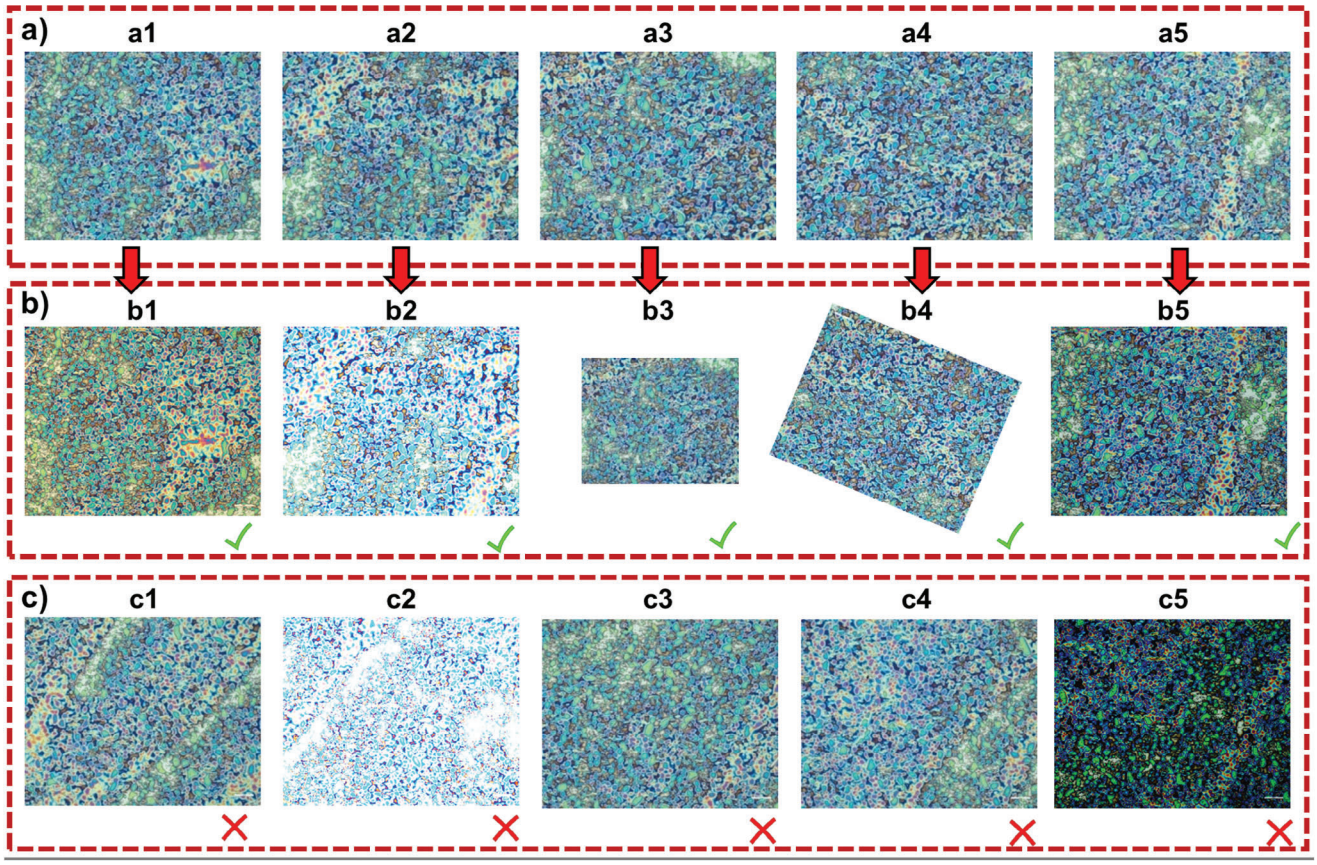

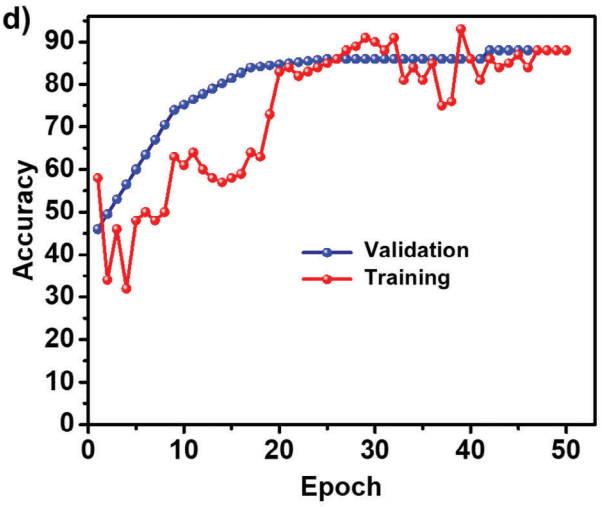

e)

	Accuracy
Brightness	95.0
Size	90.9
Rotation	92.3

Figure 4. Authentication of structurally colored PUFs via a CNN-based algorithm. a) Bright-field optical images of genuine security labels in the database (a1-a5). b) Bright-field optical images taken under different conditions from five genuine labels. Images of different brightnesses (b1, b2, b5), reduced size (b3), rotation (b4). c) Bright-field optical images of fake security labels that are not in the database (c1-c5). d) Accuracy of the training and validation process of structurally colored PUFs. e) Accuracy rates for identifying genuine samples using images taken under varied brightness, sizing, and rotation conditions.

of 5 × 5 pixels were selected at known locations in each image for genuine (**Figure** 5a) and fake (Figure 5b) labels. Visual inspection of these pixels can qualitatively inform about the similarity between labels. To quantitatively prove the color difference, the colors in these regions were analyzed on a pixel basis and color-matching percentage values were calculated (see supporting information for details) using Haralick feature extraction algorithm.[71] Figure 5c shows that the color-matching percentages were typically close to 100 for the genuine labels, whereas the fake label was unable to exceed 20%. This quantitative

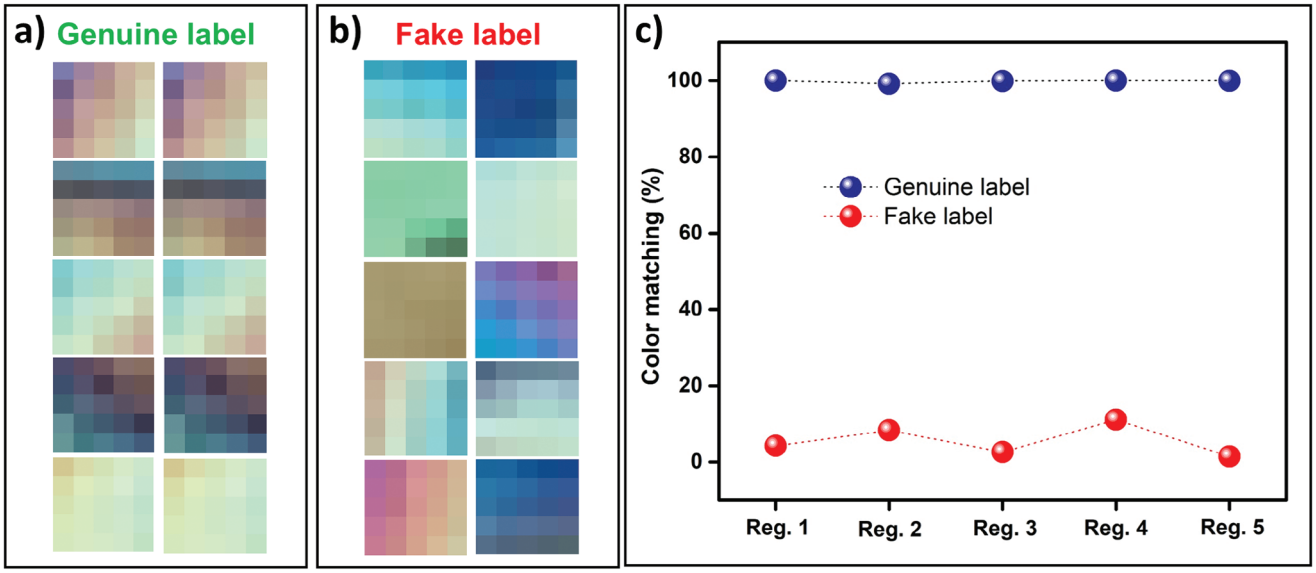

Figure 5. Color matching. a,b) Bright-field optical microscopy images with a size of 5 × 5 pixels obtained from 5 different regions. The left columns represent the images from the database and the right column shows the images taken from a) genuine and b) fake labels. c) Color matching percentage calculated from these 5 regions for genuine and fake labels.

color matching enables direct analysis of color information for authentication and for probing the stability of the features, as discussed later.

2.3. Encoding Capacity of Structurally Colored ZnO PUFs

To calculate the encoding capacity (R^n), there is a need to extract the number of responses and pixels in a bright-field optical image of structurally colored ZnO features. The theoretical upper limit for R is 256^3, accounting for the 256 possible values of the red, green, and blue (RGB) components. A computational procedure[35] was employed to analyze the actual number of distinguishable colors and the distribution of RGB values in the images (see supporting information for details). The color of each pixel was determined according to the values of the RGB components, and the color values of the pixels were recorded in a matrix to determine the number of unique colors. This matrix is referred to as the data matrix, where each row corresponds to a pixel. Unique rows in the matrix represent the colors that appear only once. In this way, the total number of colors in the image could be calculated by taking the size of the matrix. **Figure 6** presents the RGB distribution of 4 samples for images with pixel sizes of 2752 × 2208 and 512 × 512. The stochastic nature of the process results in variations in the thicknesses of features and random shadowing effects, which together result in differences in the RGB distribution and total number of distinguishable colors. Consequently, each sample exhibits a distinct and unclonable color distribution, which can be utilized as a security layer in the authentication. The achievable number of colors was significantly higher for the images with larger pixel sizes due to the greater area allowing enhanced color combinations. The R-value was as high as 6.4×10^5 for the images with the larger pixel size, leading to an extremely high encoding capacity of $(6.4 \times 10^5)^{(2752 \times 2208)}$. The complexity of the patterns and the rich color distribution allow for high encoding capacity, preventing the cloning of labels to provide a highly secure encryption.

2.4. Stability of Structurally Colored PUFs

A key need for applications is combining high encoding capacity in bright-field optical imaging-based PUFs with robustness. To confirm the robustness of the present ZnO-based PUFs, we studied thermal and chemical stabilities. To accurately and systematically monitor the stability of structurally colored ZnO features, we first used lithography-assisted fabrication process. In this manner, an array of features with known positions could be probed after thermal and chemical stability tests. Circular holes with a diameter of 50 µm and a pitch of 100 µm were fabricated in a photoresist film with maskless lithography on a Si substrate. The deposition of ZnO was then performed at conditions that were identical to the ones used for PUFs. Afterward, the photoresist was removed by dissolving in an organic solvent to reveal structurally colored ZnO features. Chemical stability tests were performed by immersion in pure water, chloroform, chlorobenzene, propanol, and acetone for 5 min each (**Figure 7a**). Optical microscopy images were taken before and after the test, and these images were extracted from each other with the help of a computational process to compare their differences. When the similarity ratios were analyzed, it was found that they showed over 99% similarity, proving that the PUF samples were highly stable against aggressive solvents. The thermal stability of the ZnO film was probed at different temperatures with a treatment time of 30 min for each temperature (Figure 7b). When the optical images before and after the test are compared, there is no degradation observed in its structure even when subjected to thermal treatment at 500 °C. When the difference between the images before and after the thermal treatment was analyzed, 97.65% similarity was determined. As a result, the current structurally

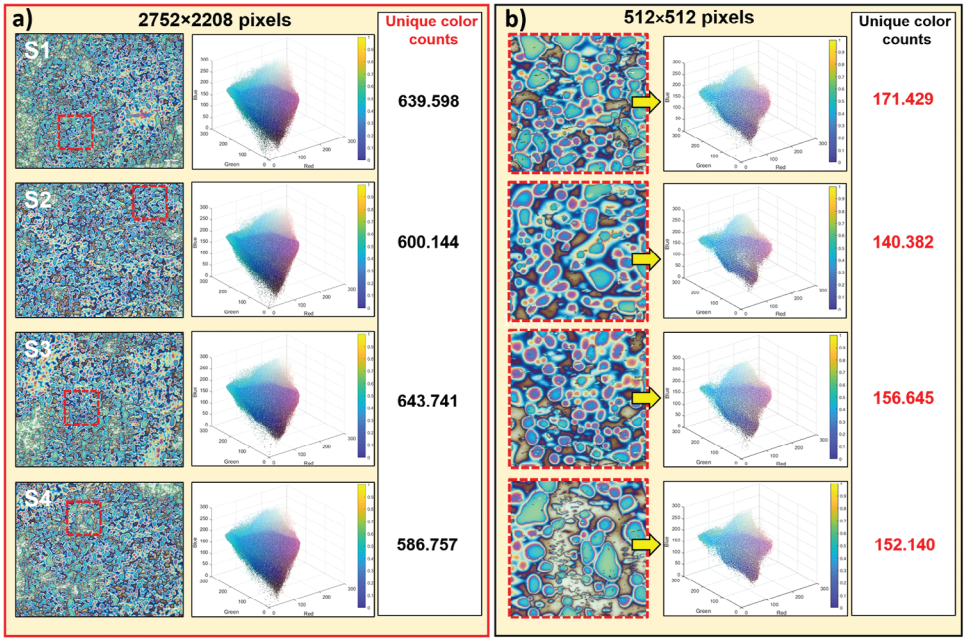

Figure 6. Image analysis for the calculation of the encoding capacity. The optical microscopy images, distribution of RGB values, and the number of responses R) for different samples with a size of images a) 2752 × 2208 pixels and b) 512 × 512 pixels.

colored ZnO films have been shown to maintain their stability even under extreme challenges.

To further probe the thermal and chemical stability of PUFs, we performed experiments on randomly positioned and structurally colored ZnO features. Figure 7c presents bright-field optical microscopy images of the sample before and after thermal annealing at 500 °C for 30 min. To quantitatively measure the changes in the spatial and color distribution of the ZnO features, feature matching (Figure 7e) and color matching (Figure 7f) percentages were calculated by using the images taken at the same locations of the sample before and after the stability test. After thermal annealing, 96.07% of the features can be successfully matched. To probe the stability of structural color, 10 regions with a size of 5 × 5 pixels were selected (Figure 7d). The color-matching percentages were higher than 80% for all conditions. The chemical stability was studied by dipping the PUF samples in solutions of varying pH values of 4, 7, and 10 for 1 min (Figures S10–S13, Supporting Information). In neutral and basic conditions, more than 99% of the features and 90% of the colors could be effectively retained. At pH 4, there was slight reduction in the feature and color-matching percentages due to the partial dissolution of ZnO in the acidic condition. Results confirm the unique thermal and chemical robustness of the structurally colored PUFs.

Collectively, the presented approach simultaneously addresses extreme levels of encoding capacity and robustness in a bright-field optical resolvability. As a straightforward comparison of the performance of the presented system with the state-of-the-art in the literature, Figure 1h compares the maximum operating temperatures of the system along with the number of responses, R. This comparison uses the R-value rather than the encoding capacity, since the number of pixels, and therefore the encoding capacity calculation, greatly varies in the literature, hindering reasonable comparisons. Even though there are studies reporting high-temperature stability, these studies have R values that are orders of magnitude smaller than the one reported in our present work. Similar comparison plots can also include mechanical and chemical stability; however, the lack of systematic tests in the literature challenges the construction of such comparisons. The stability of an encoding system at temperatures as high as 500 °C is significant for two reasons. First, thermal stability at elevated temperatures, reaching several hundred degrees Celsius, demonstrates the robustness of the material system and indicates a high thermodynamic barrier to degradation. For example, accelerated aging studies at elevated temperatures are commonly used in industry to test the long-term durability of materials at ambient temperatures. Second, certain niche but sensitive applications would benefit from this robustness at elevated temperatures.

3. Conclusion

This study has presented an effective strategy to construct PUFs with four key attributes. First extremely rich structural color generation ensures very high encoding capacity and construction of a strong PUF. This high encoding capacity optical PUF can be read out using bright-field optical imaging including smartphones that are broadly available. The stable operation at a high encoding capacity beyond the state of the art emerges from the choice of robust materials. The entire process is stochastic, scalable, and amenable to constructing hybrid encoding systems with deterministic and stochastic components. Deep learning-based algorithms effectively authenticate the chaotic features with extremely rich encoding capacity. This study critically addresses the dilemma of high encoding capacity, bright-field resolvability, and stability through the design and fabrication of PUFs using robust inorganic materials and practical fabrication methods. This work

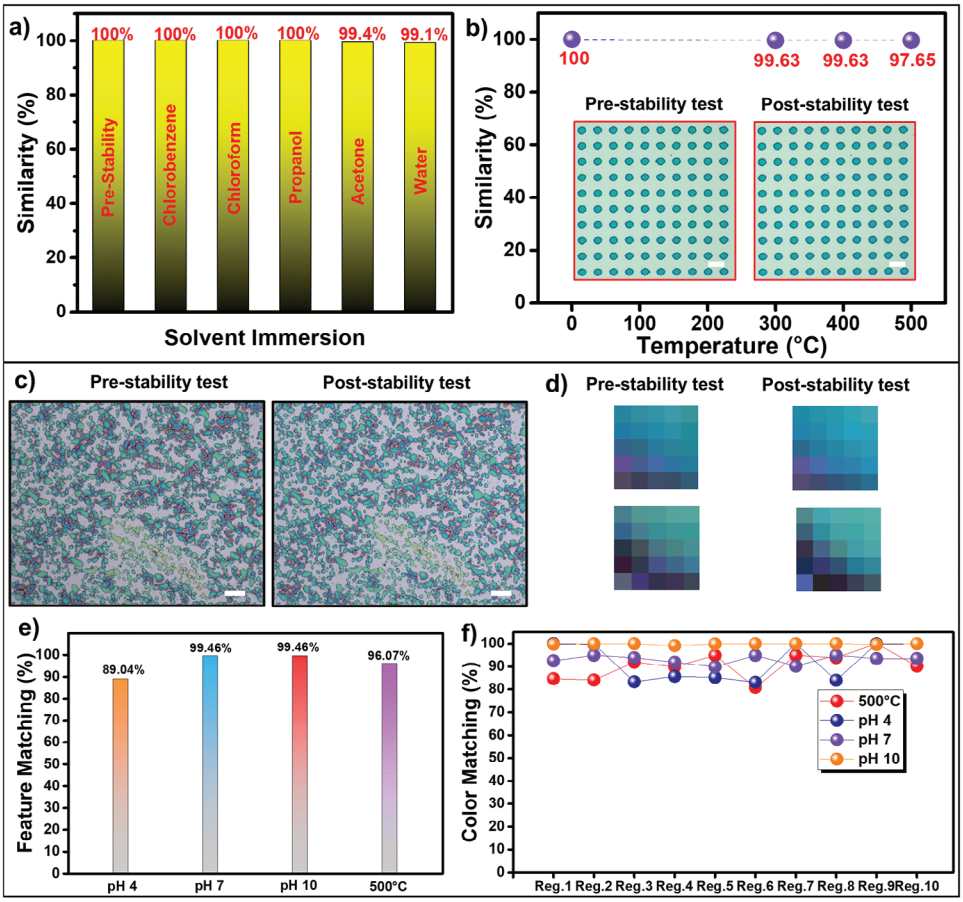

Figure 7. Stability of structurally colored PUFs. a) The solvent and b) thermal stability of lithographically patterned ZnO features based on the similarity ratios derived from the optical microscopy images taken before and after the test. Optical microscopy images of lithographically patterned ZnO features before and after the thermal stability test are given inside the graph. c) Optical microscopy images of randomly positioned and colored ZnO features before and after the thermal stability test at 500 °C. d) Images with a size of 5 × 5 pixels obtained from 2 different regions. The left and right columns represent the images before and after the thermal stability test, respectively. e) Feature matching and f) color matching percentages for the chemical and thermal stability tests. Scale bars are 100 µm.

can stimulate activity regarding the expansion of the material composition, response mechanism, and substrate-independent structural coloration.

4. Experimental Section

Materials: Si wafers (⟨100⟩, N/Phos) were purchased from University Wafer. AZ1518 positive-tone photoresist was purchased from Kayaku Advanced Materials. Ammonium peroxodisulphate, acetone, and 2-propanol were purchased from Merck. Chloroform and chlorobenzene were purchased from Sigma-Aldrich. Purified water was used throughout the experiments. PC (Mw ≈26000) was purchased from Macklin Biochemical Co., Ltd. Cu foil (MT18Ex) was purchased from Mitsui Kinzoku Co., Ltd. AgNPs with a diameter of 5 nm and concentration of 0.1 mg mL^{-1} was purchased from Nanjing XFNANO Materials TECH Co.Ltd. Hydrogen peroxide was purchased from Tianjin Jiangtian Chemical Technology Co., Ltd.

Fabrication of Structurally Colored PUFs: The randomly distributed domains with varied size, geometry, and color response were generated in three steps. In the first step, porous membranes were prepared by a stochastic photothermal process, followed by transfer onto a target substrate. In the final step, ZnO films of varied thicknesses were deposited via PVD. Details of each step are given below.

Preparation of Porous Membranes: A PC solution was prepared by dissolving 1 mg of PC in 99 mg of solvent mixture of dichloromethane and cyclohexanone (9:1). The PC solution was then spin-coated on Cu foil at a spinning speed of 4000 rpm to form a thin membrane. AgNPs suspension was diluted to 10 µg mL^{-1} by water and ethanol (1:1) and dispersed on the resulting PC membrane at 400 rpm. After solvent volatilization, the AgNPs that were irradiated by an IPL system (Model S-2100, Xenon Co., Ltd.) under an energy level of 1365.25 J for ten times at a pulse width of 1 ms and an interval of 1.5 s. Finally, the AgNPs on the membrane were removed by hydrogen peroxide to yield a porous PC membrane.

Transfer of Porous Membranes onto a Target Substrate: The Cu foil under the porous membrane was removed by immersing the membrane into an aqueous solution of 0.5 M ammonium peroxodisulfate for 7 h. As a result of the dissolution of the foil, the membrane remained suspended in the solution due to surface tension, maintaining its structural integrity. The free-standing membrane was then transferred onto the silicon substrate and then dried at 40 °C for 5 min.

Deposition of ZnO Films: ZnO thin films were deposited on a silicon substrate using RF magnetron sputtering with a NANOVAK NVTS-400 system. The deposition process employed a ZnO target and 99.999% pure Ar gas. The Si substrates underwent a cleaning process involving sequential ultrasound agitation in acetone, isopropyl alcohol, and ethanol, followed by drying with nitrogen gas. The samples were further cleaned using a UV–ozone system for 20 min. This cleaning procedure aimed to eliminate

hydrocarbon residues and enhanced the adhesion of the ZnO. Before initiating the deposition process, the chamber was purged to achieve a base pressure of 2×10^{-6} Torr. The deposition was performed under a pressure of 3.9 mTorr, argon flow rate of 12 sccm, and RF power of 80 W at room temperature. ZnO thin films with thicknesses of 160, 180, 200, 210, 250, and 290 nm were deposited at a rate of 0.5 nm s^{-1}. Throughout the deposition process, the thickness and deposition rate were meticulously monitored using quartz crystal microbalance thickness measuring equipment manufactured by Inficon.

To generate multi-color PUFs, the PVD process was sequentially performed using the porous PC membrane as the stencil mask that can transfer patterns defined by the holes to the underneath Si substrate (Figure S1, Supporting Information). A 160 nm thick ZnO film was deposited as the first layer. Following the removal of the first stencil mask, another porous PC membrane with stochastically defined pores was transferred onto the Si substrate. A 150 nm thick ZnO film was then deposited and patterned following the same procedure as the first layer. The above stencil mask placement and PVD deposition processes can be repeated several times to yield a multicolored heterogeneous surface with varying thicknesses due to pores at random positions.

Characterization: An upright research microscope (Axio Imager 2, ZEISS) was used to acquire optical images of the samples. The morphology and thickness of the ZnO films were probed by top-down and cross-sectional SEM imaging using EVO LS10 (ZEISS) at 25 kV. Elemental analysis of the features was characterized using EDX (Bruker). Thin film XRD data were recorded using a diffractometer (Bruker AXS D8) operating at a scanning step of 0.1° in the 2θ range of 5–90° using a Cu Kα radiation source. The UV–vis diffuse reflectance spectrum of the ZnO metal oxide film thickness was measured via a Shimadzu UV-3600i Plus spectrophotometer using an ISR-603 integrating sphere. While the spectra were taken, the angle of incidence of the light source at 310 nm wavelength was determined at 8° and the slit width was set as 20 nm. In addition, the spectrum was obtained in a wavelength range of 800–250 nm for 30 s. at a high scan speed module. The surface topography of ZnO films was investigated by AFM (Multimode 8, Veeco).

Simulation of Color Response: The reflectance spectra of the ZnO thin films were simulated using the generalized transfer matrix method[72] as implemented in the open-source Python package pyGTM. The spectra were calculated from 300 to 800 nm at an interval of 5 nm. The ZnO film consisted of air, ZnO, a native oxide layer (SiO_2, 2.5 nm thick), and a Si substrate. The refractive indices of crystalline Si[73] and the native oxide layer needed for the simulations were taken from the literature. The refractive index of air was set to 1. The refractive index of ZnO was taken from the work of Aguilar et al.[65] Afterward, the reflectance spectra were converted to RGB color via CIE 31 color scheme (standard illuminant D65 and 2 degrees standard observer) using open source Python package Color.

Stability: The chemical and temperature stability of PUFs were studied with multiple tests using lithographically defined and randomly positioned ZnO features. For chemical stability, a PUF sample was immersed in chlorobenzene, chloroform, propanol, acetone, and water for 5 min each under ultrasonic agitation and then dried with nitrogen. Thermal stability tests were performed in a muffle furnace by heating the samples to a temperature of up to 500 °C for 30 min at a heating rate of 10 °C per min. Chemical stability tests were performed by immersing the samples in aqueous solutions of varying pH for 1 min under ambient conditions. The pH of the solutions was adjusted using NaOH and HCl. The images of the samples before and after the test were compared by using Oriented FAST and Rotated BRIEF (ORB) feature matching algorithms. Recognition scores were calculated by evaluating the successful matching of feature points. Color-matching percentages were calculated as described in the supporting information.

To quantify the morphological evolution of identical features during the stability tests, lithographically defined ZnO features were fabricated. A 2 µm thick film of AZ1518 positive-tone photoresist was spin-coated on a cleaned Si substrate at 4000 rpm. After coating, the substrates were subjected to a soft bake at 65 °C for 3 min. Subsequently, an array of circular features with a diameter of 50 µm and pitch of 50 µm was written using laser lithography (Kloe, Dilase 250). Unexposed photoresist regions were removed by washing in the AZ developer. Following drying, a hard-bake was performed at 95 °C for 90 s.

Deep Learning Based Authentication: Optical microscopy was used to acquire 1000 images of structurally colored PUFs. These images were taken at different magnification, brightness, and rotation conditions. According to these conditions, a deep convolutional network with Resnet-50 architecture was implemented using MATLAB to extract and classify random patterns in these images.[74] Then, 20% of these images were used for validation, while the remaining 80% were used for training.[75] BoF technique was used to extract features from the training images.[43] A series of operations were performed using CNNs to recognize and decode structurally colored PUFs. After each learning cycle for validation, the images were sent to the engine for testing and a training accuracy plot was extracted. After completing the learning cycle, PUFs were matched.

Encoding Capacity of Structurally Colored PUFs: The encoding capacity was calculated by using R^n. Here R refers to the number of color responses that could be detected under bright-field optical microscopy imaging. The theoretical upper limit for R refers to $256 \times 256 \times 256$ that spans the entire RGB) color space. The actual R-value was extracted from the images with the assistance of MATLAB software from images with a pixel size of 512×512.

Statistical Analysis: The randomness analysis was conducted using binary keys derived from 30 images obtained from multiple samples. A *p*-value threshold of $\geq$0.01 was employed to ascertain the randomness of the binary keys.

Supporting Information

Supporting Information is available from the Wiley Online Library or from the author.

Acknowledgements

A.E. and M.R. contributed equally to this work. The authors are grateful for the financial support of the Unit of the Scientific Research Projects of Erciyes University (FDK-2023-12660). AE acknowledges the financial support from the Scientific and Technological Research Council of Turkey (2211-C TUBITAK), X. H acknowledges the support from the Key Research and Development Program of Zhejiang Province under grant no. 2021C05005, 2021C05007-2, and the National Natural Science Foundation of China under grant no. 52121002 and 62371335.

Conflict of Interest

The authors declare no conflict of interest.

Data Availability Statement

The data that support the findings of this study are available from the corresponding author upon reasonable request.

Keywords

anti-counterfeiting, physically unclonable functions, structural color, thin films, zinc oxide

Received: September 20, 2024
Revised: November 7, 2024
Published online: December 10, 2024

[1] R. Arppe, T. J. Sørensen, *Nat. Rev. Chem.* **2017**, *14*, 1.
[2] D. Collon, *First Impressions: Cylinder Seals in the Ancient Near East*, 1st paperback ed., British Museum Publications, London, **1993**, https://www.amazon.com/First-Impressions-Cylinder-Seals-Ancient/dp/0714111368.
[3] R. Pappu, B. Recht, J. Taylor, N. Gershenfeld, *Science* **2002**, *297*, 2026.
[4] T. McGrath, I. E. Bagci, Z. M. Wang, U. Roedig, R. J. Young, *Appl. Phys. Rev.* **2019**, *6*, 11303.
[5] N. B. Kiremitler, A. Esidir, G. A. Drake, A. F. Yazici, F. Sahin, I. Torun, M. Kalay, Y. Kelestemur, H. V. Demir, M. Shim, E. Mutlugun, M. S. Onses, *Adv. Opt. Mater.* **2023**, 2302464.
[6] Y. Liu, F. Han, F. Li, Y. Zhao, M. Chen, Z. Xu, X. Zheng, H. Hu, J. Yao, T. Guo, W. Lin, Y. Zheng, B. You, P. Liu, Y. Li, L. Qian, *Nat. Commun.* **2019**, *10*, 1.
[7] Y. Liu, Y. Zheng, Y. Zhu, F. Ma, X. Zheng, K. Yang, X. Zheng, Z. Xu, S. Ju, Y. Zheng, T. Guo, L. Qian, F. Li, *ACS Appl. Mater. Interfaces* **2020**, *12*, 39649.
[8] Q. Li, F. Chen, J. Kang, J. Su, F. Huang, P. Wang, X. Yang, Y. Hou, *Adv. Funct. Mater.* **2021**, *31*, 2010537.
[9] A. F. Smith, P. Patton, S. E. Skrabalak, *Adv. Funct. Mater.* **2016**, *26*, 1315.
[10] Z. Zhao, X. Wang, L. Zhang, J. Song, J. Liao, H. Wang, J. Xu, *Adv. Mater. Technol.* **2023**, *8*, 2301055.
[11] N. Kayaci, R. Ozdemir, M. Kalay, N. B. Kiremitler, H. Usta, M. S. Onses, *Adv. Funct. Mater.* **2022**, *32*, 2108675.
[12] S. Lee, S. Pekdemir, N. Kayaci, M. Kalay, M. S. Onses, J. Ye, *ACS Appl. Mater. Interfaces* **2023**, *15*, 33878.
[13] A. Esidir, S. Pekdemir, M. Kalay, M. S. Onses, *ACS Appl. Mater. Interfaces* **2024**, *16*, 16532.
[14] A. Esidir, N. Kayaci, N. B. Kiremitler, M. Kalay, F. Sahin, G. Sezer, M. Kaya, M. S. Onses, *ACS Appl. Mater. Interfaces* **2023**, *15*, 41373.
[15] A. Esidir, N. B. Kiremitler, M. Kalay, A. Basturk, M. S. Onses, *ACS Appl. Polym. Mater.* **2022**, *4*, 5952.
[16] N. Torun, I. Torun, M. Sakir, M. Kalay, M. S. Onses, *ACS Appl. Mater. Interfaces* **2021**, *13*, 11247.
[17] H. J. Bae, S. Bae, C. Park, S. Han, J. Kim, L. N. Kim, K. Kim, S. H. Song, W. Park, S. Kwon, *Adv. Mater.* **2015**, *27*, 2083.
[18] M. R. Carro-Temboury, R. Arppe, T. Vosch, T. J. Sørensen, *Sci. Adv.* **2018**, *4*, 1701384.
[19] Y. Gu, C. He, Y. Zhang, L. Lin, B. D. Thackray, J. Ye, *Nat. Commun.* **2020**, *11*, 516.
[20] D. J. Crandall, S. E. Skrabalak, J. D. Smith, M. A. Reza, N. L. Smith, J. Gu, M. Ibrar, *ACS Nano* **2021**, *15*, 2901.
[21] M. Moglianetti, D. Pedone, P. Morerio, A. Scarsi, P. Donati, M. Bustreo, A. Del Bue, P. P. Pompa, *ACS Appl. Mater. Interfaces* **2022**, *14*, 25898.
[22] M. S. Kim, G. J. Lee, *ACS Appl. Mater. Interfaces* **2023**, *15*, 4477.
[23] R. Arppe-Tabbara, M. Tabbara, T. J. Sørensen, *ACS Appl. Mater. Interfaces* **2019**, *11*, 6475.
[24] W. Hong, Z. Yuan, X. Chen, W. Hong, Z. Yuan, X. Chen, *Small* **2020**, *16*, 1907626.
[25] L. Tian, K. K. Liu, M. Fei, S. Tadepalli, S. Cao, J. A. Geldmeier, V. V. Tsukruk, S. Singamaneni, *ACS Appl. Mater. Interfaces* **2016**, *8*, 4031.
[26] Y. Geng, J. Noh, I. Drevensek-Olenik, R. Rupp, G. Lenzini, J. P. F. Lagerwall, *Sci. Rep.* **2016**, *6*, 26840.
[27] S. Nocentini, U. Rührmair, M. Barni, D. S. Wiersma, F. Riboli, *Nat. Mater.* **2024**, *23*, 369.
[28] F. Han, Y. Liu, F. Li, Y. Lu, H. Cheng, Y. Lin, T. Zhao, S. H. Ng, U. Bach, Y. Zheng, *J. Mater. Chem. C* **2019**, *7*, 13040.
[29] X. He, Y. Gu, B. Yu, Z. Liu, K. Zhu, N. Wu, X. Zhao, Y. Wei, J. Zhou, Y. Song, *J. Mater. Chem. C* **2019**, *7*, 14069.
[30] Y. Li, Z. Liu, K. Zhu, L. Ai, P. Jia, N. Wu, H. Yu, J. Wang, X. Yao, J. Zhou, Y. Song, Y. H. Li, P. Jia, N. Wa, H. T. Yu, J. M. Zhou, Z. W. Liu, K. Zhu, J. Q. Wang, L. Q. Ai, X. Yao, *Adv. Mater. Interfaces* **2021**, *8*, 2101281.
[31] Y. Li, Y. Mao, J. Wang, Z. Liu, P. Jia, N. Wu, H. Yu, J. Wang, Y. Song, J. Zhou, *Nanoscale* **2022**, *14*, 8833.
[32] S. Jiang, S. H. Kim, C. S. Park, W. Bin Lee, S. S. Lee, *ACS Appl. Mater. Interfaces* **2022**, *14*, 39240.
[33] V. Lapidas, A. Zhizhchenko, E. Pustovalov, D. Storozhenko, A. Kuchmizhak, *Appl. Phys. Lett.* **2022**, *120*, 261104.
[34] J. Wu, X. Liu, X. Liu, Z. Tang, Z. Huang, W. Lin, X. Lin, G. Yi, *Chem. Eng. J.* **2022**, *439*, 135601.
[35] J. Wu, J. Li, X. Liu, L. Gong, J. Chen, Z. Tang, W. Lin, Y. Mu, X. Lin, W. Hong, G. Yi, X. Chen, *ACS Appl. Mater. Interfaces* **2022**, *14*, 2369.
[36] Y. Gao, K. Ge, Z. Zhang, Z. Li, S. Hu, H. Ji, M. Li, H. Feng, Y. Gao, K. Ge, Z. Zhang, Z. Li, H. Feng, S. Hu, H. Ji, M. Li, *Adv. Sci.* **2024**, *11*, 2305876.
[37] X. Lin, Q. Li, Y. Tang, Z. Chen, R. Chen, Y. Sun, W. Lin, G. Yi, Q. Li, *Adv. Sci.* **2024**, *11*, 2401983.
[38] F. Wang, R. Lyu, H. Xu, R. Gong, B. Ding, *Respons. Mater.* **2024**, *2*, 20240007.
[39] T. Hu, S. Zhang, Y. Qi, *Small* **2024**, https://onlinelibrary.wiley.com/doi/abs/10.1002/smll.202405243.
[40] B. A. Rorem, T. H. Cho, N. Farjam, J. D. Lenef, K. Barton, N. P. Dasgupta, L. J. Guo, *ACS Appl. Mater. Interfaces* **2022**, *14*, 31099.
[41] H. Liu, D. Quan, K. Li, Y. Zheng, F. Lou, S. Liu, Y. Liu, A. Kumar Srivastava, G. Li, C. Qiu, Z. Liu, X. Cheng, H. Liu, K. Li, Y. Liu, C. Qiu, Z. Liu, D. Quan, Y. Zheng, F. Lou, G. Li, X. Cheng, A. K. Srivastava, S. Liu, *Adv. Opt. Mater.* **2021**, *9*, 2001670.
[42] M. Ren, T. Li, W. Huo, Y. Guo, Z. Xia, Y. Li, J. Niu, M. S. Onses, X. Huang, *Int. J. Smart Nano Mater.* **2023**, *14*, 391.
[43] G. Csurka, C. R. Dance, L. Fan, J. Willamowski, C. Bray, *Workshop on statistical learning in computer vision* **2004**, *1*, 1.
[44] Y.-W. Hu, T.-P. Zhang, C.-F. Wang, K.-K. Liu, Y. Sun, L. Li, C.-F. Lv, Y.-C. Liang, F.-H. Jiao, W.-B. Zhao, L. Dong, C.-X. Shan, Y. Hu, K. Liu, Y. Sun, L. Li, C. Lv, Y. Liang, F. Jiao, W. Zhao, L. Dong, C. Shan, T. Zhang, C. Wang, *Adv. Funct. Mater.* **2021**, *31*, 2102108.
[45] P. Chen, D. Li, Z. Li, X. Xu, H. Wang, X. Zhou, T. Zhai, *ACS Nano* **2023**, *17*, 23989.
[46] M. S. Kim, G. J. Lee, J. W. Leem, S. Choi, Y. L. Kim, Y. M. Song, *Nat. Commun.* **2022**, *13*, 247.
[47] M. Kalay, A. Esidir, M. Ruzi, N. B. Kiremitler, M. S. Onses, *Eur. Polym. J.* **2024**, *202*, 112598.
[48] X. Gong, Z. Qiao, Y. Liao, S. Zhu, L. Shi, M. Kim, Y.-C. Chen, X. Gong, Z. Qiao, Y. Liao, S. Zhu, M. Kim, Y.-C. Chen, L. Shi, *Adv. Mater.* **2022**, *34*, 2107809.
[49] J. Wang, Q. Zhang, R. Chen, J. Li, J. Wang, G. Hu, M. Cui, X. Jiang, B. Song, Y. He, *Nano Today* **2021**, *41*, 101324.
[50] Z. C. Meijs, H. S. Yun, P. Fandre, G. Park, D. K. Yoon, L. Isa, *ACS Appl. Mater. Interfaces* **2023**, *15*, 53053.
[51] T. Zhang, L. Wang, J. Wang, Z. Wang, M. Gupta, X. Guo, Y. Zhu, Y. C. Yiu, T. K. C. Hui, Y. Zhou, C. Li, D. Lei, K. H. Li, X. Wang, Q. Wang, L. Shao, Z. Chu, *Nat. Commun.* **2023**, *14*, 1.
[52] Y. Lu, H. Chen, H. Cheng, H. Qiu, C. Jiang, Y. Zheng, *ACS Appl. Nano Mater.* **2022**, *5*, 9298.
[53] J. Park, J. W. Leem, M. Park, J. O. Kim, Z. Ku, W. Chegal, S. W. Kang, Y. L. Kim, *ACS Nano* **2024**, *18*, 1041.
[54] N. Sun, Z. Chen, Y. Wang, S. Wang, Y. Xie, Q. Liu, *Nat. Commun.* **2023**, *14*, 1.
[55] L. Jing, H. Si, T. Chen, L. Y. Hsiao, H. Yang, J. M. Little, K. Li, S. Li, Q. Xie, P. Y. Chen, *Adv. Mater. Technol.* **2023**, *8*, 2300568.
[56] O. Szabó, S. Kováčová, V. Tvarožek, I. Novotný, P. Šutta, M. Netrvalová, D. Rossberg, P. Schaaf, *Thin Solid Films* **2015**, *591*, 230.
[57] F. Foadi, N. Celik, A. Esidir, M. S. Onses, *Surf. Coatings Technol.* **2024**, *483*, 130749.
[58] R. Nandi, S. K. Appani, S. S. Major, *J. Appl. Phys.* **2017**, *121*, 215306.
[59] E. S. Ameh, *Int. J. Adv. Manuf. Technol.* **2019**, *105*, 3289.

[60] J. H. Lee, M. J. Choi, S. M. Kang, H. Il Eum, G. H. Kim, *ACS Appl. Nano Mater.* **2024**, *7*, 8655.
[61] Z. Dong, J. Ho, Y. F. Yu, Y. H. Fu, R. Paniagua-Dominguez, S. Wang, A. I. Kuznetsov, J. K. W. Yang, *Nano Lett.* **2017**, *17*, 7620.
[62] C. W. Moon, J. E. Park, M. Park, Y. Kim, K. Narasimha, J. K. Hyun, S. J. Park, *ACS Appl. Mater. Interfaces* **2021**, *13*, 1555.
[63] J. E. Park, S. Lee, Y. Kim, S. K. Albert, Y. Lee, J. K. Hyun, W. Lee, S. J. Park, *ACS Appl. Mater. Interfaces* **2023**, *15*, 51753.
[64] J. Geng, L. Xu, W. Yan, L. Shi, M. Qiu, *Nat. Commun.* **2023**, *14*, 565.
[65] O. Aguilar, S. De Castro, M. P. F. Godoy, M. Rebello, S. Dias, *Opt. Mater. Express* **2019**, *9*, 3638.
[66] D. Choi, C. K. Shin, D. Yoon, D. S. Chung, Y. W. Jin, L. P. Lee, *Nano Lett.* **2014**, *14*, 3374.
[67] S. Sun, Z. Zhou, C. Zhang, Y. Gao, Z. Duan, S. Xiao, Q. Song, *ACS Nano* **2017**, *11*, 4445.
[68] B. Yang, W. Liu, Z. Li, H. Cheng, D. Y. Choi, S. Chen, J. Tian, *Nano Lett.* **2019**, *19*, 4221.
[69] A. Krizhevsky, I. Sutskever, G. E. Hinton, *Commun. ACM* **2017**, *60*, 84.
[70] J. Sánchez, F. Perronnin, Proc. IEEE Comput. Soc. Conf. Comput. Vis. Pattern Recognit, Colorado Springs, CO, USA **2011**, 1665–1672.
[71] A. Porebski, N. Vandenbroucke, L. Macaire, Haralick feature extraction from LBP images for color texture classification, 2008 First Workshops on Image Processing Theory, Tools and Applications, Sousse, Tunisia **2008**, *2008*, 1–8.
[72] N. C. Passler, A. Paarmann, *J. Opt. Soc. Am. B* **2017**, *34*, 2128.
[73] C. Schinke, P. Christian Peest, J. Schmidt, R. Brendel, K. Bothe, M. R. Vogt, I. Kröger, S. Winter, A. Schirmacher, S. Lim, H. T. Nguyen, D. Macdonald, *AIP Adv.* **2015**, *5*, 67168.
[74] S. Adige, R. Kurban, A. Durmuş, E. Karaköse, *Neural Comput. Appl.* **2023**, *35*, 12073.
[75] D. Nistér, H. Stewénius, *Proc. IEEE Comput. Soc. Conf. Comput. Vis. Pattern Recognit.* **2006**, *2*, 2161.